FULL PAPER

Harvesting Lost Photons: Plasmon and Upconversion Enhanced Broadband Photocatalytic Activity in Core@Shell Microspheres Based on Lanthanide-Doped NaYF$_4$, TiO$_2$, and Au

Zhenhe Xu, Marta Quintanilla, Fiorenzo Vetrone, Alexander O. Govorov, Mohamed Chaker, and Dongling Ma*

Efficiently harvesting solar energy for photocatalysis remains very challenging. Rational design of architectures by combining nanocomponents of radically different properties, for example, plasmonic, upconversion, and photocatalytic properties, offers a promising route to improve solar energy utilization. Herein, the synthesis of novel, plasmonic Au nanoparticle decorated NaYF$_4$:Yb^{3+}, Er^{3+}, Tm^{3+}-core@porous-TiO$_2$-shell microspheres is reported. They exhibit high surface area, good stability, broadband absorption from ultraviolet to near infrared, and excellent photocatalytic activity, significantly better than the benchmark P25 TiO$_2$. The enhanced activity is attributed to synergistic effects from nanocomponents arranged into the nanostructured architecture in such a way that favors the efficient charge/energy transfer among nanocomponents and largely reduced charge recombination. Optical and energy-transfer properties are modeled theoretically to support our interpretations of catalytic mechanisms. In addition to yielding novel materials and interesting properties, the current work provides physical insights that can contribute to the future development of plasmon-enhanced broadband catalysts.

1. Introduction

Porous core@shell structured materials, which consist of different functional components integrated into a single structural unit, have attracted considerable attention because of their unique properties and widespread applications in drug delivery, catalysis, waste removal, sensors, photonics, and so on.[1–4] Despite recent progress, it remains a critical challenge to create uniform core@shell structures with highly functional inner core and porous outer shell by a simple approach.

Titanium dioxide (TiO$_2$) has been a semiconductor material of significant research interest due to its fascinating features, such as nontoxicity, good chemical and thermal stability, and excellent electronic, optical, and catalytic properties,[5,6] which render it a greatly promising material in photocatalysis for the removal of inorganic and organic pollutants,[7] and for hydrogen generation,[8] as well as in dye-sensitized solar cells.[9] However, TiO$_2$ has a bandgap of 3.0–3.2 eV, and mainly absorbs ultraviolet (UV) light, which accounts for only ≈5% of the incoming solar energy.[10,11] Therefore, photons with energy lower than the band gap energy of TiO$_2$, that is, more than 90% of the solar energy, cannot be harvested for photocatalysis. Furthermore, the fast recombination of charge carriers significantly reduces the catalytic activity in practical applications. To resolve these problems, much effort, including metal-ion, and nonmetal doping,[12] dye sensitization,[13] and coupling with narrower band gap semiconductors,[14] has been undertaken toward developing the next-generation of TiO$_2$-based materials. These methods have been able to extend the absorption of TiO$_2$-based photocatalysts into the visible region to some extent and/or enhance the charge separation. However, to date, the photocatalytic performance of these materials remains poor and in general, they also suffer from thermal instability and photocorrosion, and are not environmentally friendly.[15] Therefore, it is challenging, yet highly desirable to develop a simple method for synthesizing a photocatalyst, which can absorb solar photons over a broad wavelength range and show largely improved photocatalytic activity, as well as overcome other problems mentioned above.

Au nanoparticles (NPs) show unique, size-tunable surface plasmon resonance (SPR) in the visible range, offering a new opportunity to overcome the limits of current photocatalysts.[16–18] SPR arises from collective oscillations of free electrons in plasmonic structures and is characterized by strong light absorption and/or scattering and the generation of intense

Dr. Z. Xu, Dr. M. Quintanilla, Prof. F. Vetrone,
Prof. M. Chaker, Prof. D. Ma
Institut National de la Recherche Scientifique (INRS)
Centre Énergie
Materiaux et Télécommunications
Université du Québec
1650 Boulevard Lionel-Boulet
Varennes, Québec J3X 1S2, Canada
E-mail: ma@emt.inrs.ca
Prof. A. O. Govorov
Department of Physics and Astronomy
Ohio University
Athens, OH 45701, USA

Materials
Views
www.MaterialsViews.com

ADVANCED
FUNCTIONAL
MATERIALS
www.afm-journal.de

electric fields near the surface. In principle, all these interesting features can be beneficial for photocatalysis.[10,16] Motivated by their high potential, researchers have explored the applications of plasmonic materials in the field of photocatalytic chemistry for various reactions, such as organic molecule decomposition,[19] oxidation reactions,[20,21] water splitting,[22] and considerable improvements in catalysis efficiency have been achieved. Meanwhile, from fundamental aspects, much progress has been made in understanding mechanisms for plasmon-enhanced photocatalysis. Three major underlying mechanisms have been proposed: (i) SPR induced hot electron transfer from the metal to semiconductor, (ii) enhancement in the local electromagnetic field and thus increased electron–hole pair generation rates in the semiconductor, and (iii) enhancement in scattering and thus the increase of the average photon path length in the system.[11,16,23] Nonetheless, exact mechanisms and processes in specific systems depend on the structural features and optical characteristics of individual components as well as their assemblies, and remain elusive in many cases. They can indeed be quite different case by case. In order to significantly exploit the benefits of plasmonic materials, careful and in-depth studies are required for designing plasmonic-metal/semiconductor systems and for better understanding exact pathways and critical parameters. Au NP coupled TiO_2 systems represent the most popular one of this kind. It has been found that energetic electrons formed by SPR excitation can be efficiently injected into the conduction band (CB) of TiO_2 under visible illumination.[24] In addition to favorable plasmonic effects, Au NPs can also serve as reservoir under UV irradiation for photoinduced charge carriers and extend the lifetime of electron–hole pairs.[25] All these processes require the direct contact between Au NPs and TiO_2. In this regard, tiny Au NPs free of any organic ligands on their surface, which can act as charge transfer barriers, are preferred. As reported recently, pulsed laser ablation can produce "bare and clean" Au NPs, which have been proven to facilitate catalytic reactions as the catalytically active sites on the NP surface are mostly exposed and readily accessible to reactants.[26,27] It is interesting to further apply these "bare and clean" Au NPs, with clear SPR in the visible range, to plasmon-enhanced photocatalysis.

Furthermore, as is well known, the near-infrared (NIR) light occupies about 44% of solar irradiation. Therefore, there is still plenty of room for further improvement in the capture of solar energy by harvesting NIR photons. Lanthanide-doped upconversion particles can convert longer wavelength radiation (NIR) to shorter wavelength emission (UV and/or visible). These converted UV and visible emissions can be reabsorbed by TiO_2 and Au NPs, respectively, and used for photocatalysis. Although there are a few papers reporting NIR photocatalysis driven by upconversion,[28–33] using plasmonic NPs to further improve the photocatalysis efficiency under NIR irradiation has not been demonstrated. The appropriate combination of lanthanide-doped upconverting particles and Au NPs with strongly catalytic TiO_2 into single architectures may allow the use of fascinating plasmonic and upconversion properties to efficiently harvest photons from UV, to visible and further to NIR for photocatalysis.

To this end, we report in this article, for the first time, the development of a novel hybrid photocatalyst of Au NP loaded $NaYF_4$:Yb^{3+}, Er^{3+}, Tm^{3+} (NYF)@porous-TiO_2 (denoted as NYF@TiO_2-Au) core@shell microspheres, which can improve solar energy utilization by capturing UV, visible, and NIR photons via employing the concepts of plasmonics and upconversion in the structure design. The major beneficial structural features include the intimate contact between the NYF core and TiO_2 shell and between the TiO_2 shell and Au NPs, the proximity between the Au NPs and upconverting core, as well as the porous TiO_2 network favoring easy loading of Au NPs. These outstanding features enable the efficient charge and/or energy transfer between the nanocomponents, and thus allowing the efficient realization of fascinating plasmonic and upconversion effects in photocatalysis. Moreover, the porous, open TiO_2 nanostructure offers an extra advantage. Quite different from a solid TiO_2 shell, where excitons generated in the bulk need to migrate to the surface for catalytic reactions, the porous TiO_2 shell herein allows all excitons to be created at or near the Au/TiO_2 or TiO_2/solution interfaces. As such, the charge carrier recombination is largely decreased. The photocatalytic efficiency of these new nanohybrid catalysts toward methyl orange (MO) degradation was examined, and the significant enhancement was observed with respect to the benchmark photocatalyst of Degussa P25 TiO_2, as well as NYF and NYF@TiO_2 samples. Under separate excitations of UV, visible, and NIR, optimal Au concentrations were found to be different, suggesting that exact dominant mechanisms and important factors vary in different cases. Optical and energy-transfer properties were modeled theoretically to support our interpretations of the catalytic mechanisms. In addition to yielding interesting materials and properties, the current work provides physical insights that can contribute to the future development of plasmon-enhanced broadband catalysts.

2. Results and Discussion

2.1. Microstructures

A simple and reproducible method for preparing NYF@TiO_2–Au core@porous-shell microspheres was realized by developing a step-by-step approach without involving any tricky surface functionalization steps. The fabrication process of these microspheres is schematically illustrated in **Figure 1**A. To be more specific, the following steps were taken sequentially or partially in parallel: 1) Au NPs with the average diameter of ≈5 nm (Figure S1, Supporting Information) were fabricated by laser ablation on a bulk Au target in water following our previous work;[26] 2) monodisperse NYF microspheres were prepared according to the previously reported method with some modifications.[34] The average diameter of the spheres is about 500 nm, and they are composed of tiny nanocrystals and show rough surface (Figure S2, Supporting Information); 3) porous TiO_2 was then deposited onto the NYF core to form core@shell microspheres by adapting the method for synthesizing pure TiO_2 spheres.[35] The uniform coating of porous TiO_2 around the whole surface of NYF microspheres is clearly evidenced (Figure S3A, Supporting Information). In some microspheres, empty space between the core and shell was noticed. The average size of the core@shell microspheres is
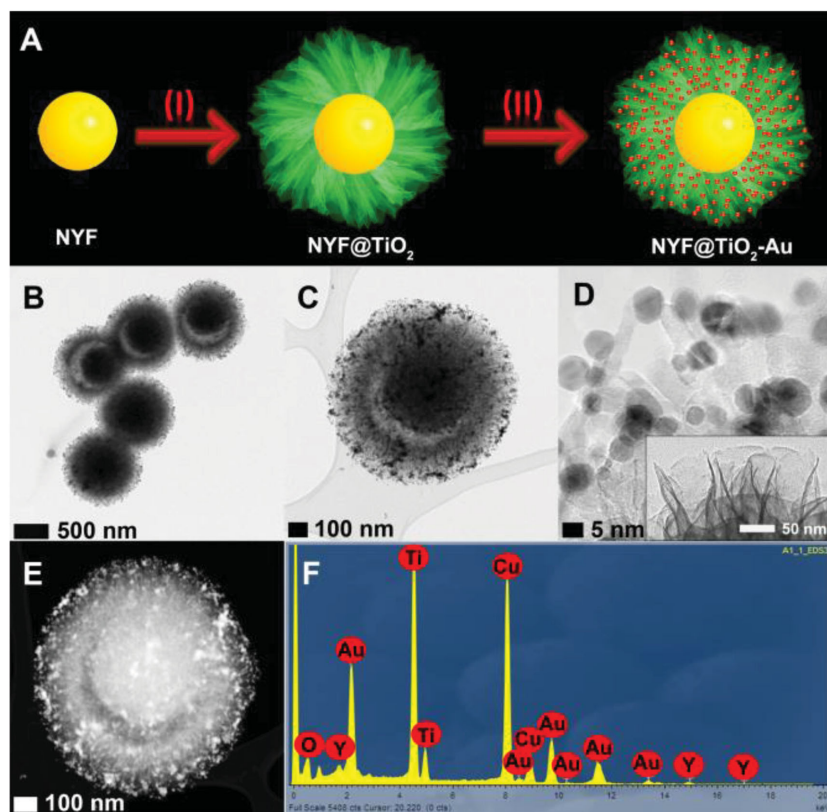
**ADVANCED
FUNCTIONAL
MATERIALS**

www.afm-journal.de

*Materials
Views*

www.MaterialsViews.com

FULL PAPER

Figure 1. A) Schematic illustration of the formation process of the NYF@TiO$_2$–Au core@shell microspheres. B,C) TEM, D) HRTEM, E) STEM, and F) EDX of the microspheres. The inset in D) shows the thin nanosheet structure of the shell.

further investigated by high-angle annular dark-field scanning transmission electron microscopy (HAADF-STEM) (Figure 1E). The core@shell structure is again clearly shown, and the Au NPs can be clearly identified because of their much higher atomic mass. The energy-dispersive X-ray (EDX) spectrum taken on a single sphere further confirms the co-existence of O, Ti, Y, and Au elements in a single architecture (Figure 1F).

The X-ray diffraction (XRD) patterns (**Figure 2**A) verify that NYF@TiO$_2$–2 wt% Au consists of hexagonal β-NaYF$_4$ and anatase TiO$_2$. Distinction between Au and other components in this complex structure by XRD technique is not easy due to the overlap of their diffraction peaks and a relatively small number of Au NPs. Zeta-potential measurements (Figure 2B) reveal that the isoelectric point (IEP) of the NYF@TiO$_2$ is about 6.35. As the pH value of the incubation solution is ≈6.0, the surface of NYF@TiO$_2$ microspheres is quite likely positively charged. Since the Au NPs are negatively charged at this pH value based on the zeta-potential measurements, the electrostatic interaction between them must contribute to the anchoring of Au NPs into the shell of the microspheres, although the contribution from hydrogen bonding cannot be absolutely excluded.[37] The chemical states of the involved elements on the surface of NYF@TiO$_2$–2 wt% Au core@shell microspheres were examined by using X-ray photoelectron spectroscopy (XPS). The full survey spectrum reveals the co-presence of Ti, O, Au, Na, Y, and F elements (Figure 2C). The high-resolution spectrum of Au4f (Figure 2D) exhibits two peaks at 84.0 eV (Au4f$_{7/2}$) and 87.6 eV (Au4f$_{5/2}$) that can be assigned to metallic Au.[38,39] The binding energies of 459.2 and 464.9 eV, ascribed to Ti2p$_{3/2}$ and Ti2p$_{1/2}$, respectively, are consistent with the typical values reported for TiO$_2$ (Figure 2E).[40] The asymmetric profile of the O1s band (Figure 2F) indicates that more than one kind of oxygen species exist. Spectral deconvolution yields two peaks, with one centered at 530.5 eV corresponding to the characteristic peak of Ti–O–Ti,[40] while the other at 532.3 eV attributed to hydroxyl radicals (H–O).

In order to compare the optical properties of NYF, NYF@TiO$_2$, and NYF@TiO$_2$–2 wt% Au, which are highly relevant to their photocatalytic behavior, the UV–vis–NIR absorption spectra were taken and compared (**Figure 3**A). NYF exhibits only one absorption band, which is located in between 910 and 1000 nm, corresponding to the $^2F_{7/2} \rightarrow ^2F_{5/2}$ transition of Yb^{3+} in the NYF host. After being coated with TiO$_2$, absorption sharply arises from 400 nm toward shorter wavelengths, characteristic of the bandgap absorption of TiO$_2$ (≈380 nm, 3.2 eV). After the Au NPs are introduced, an obvious absorption band in the visible region between 500 and 600 nm appears, characteristic of the SPR of Au NPs (Figure 3A, inset). Calculated absorption results involving porous TiO$_2$ and Au NPs are in line with
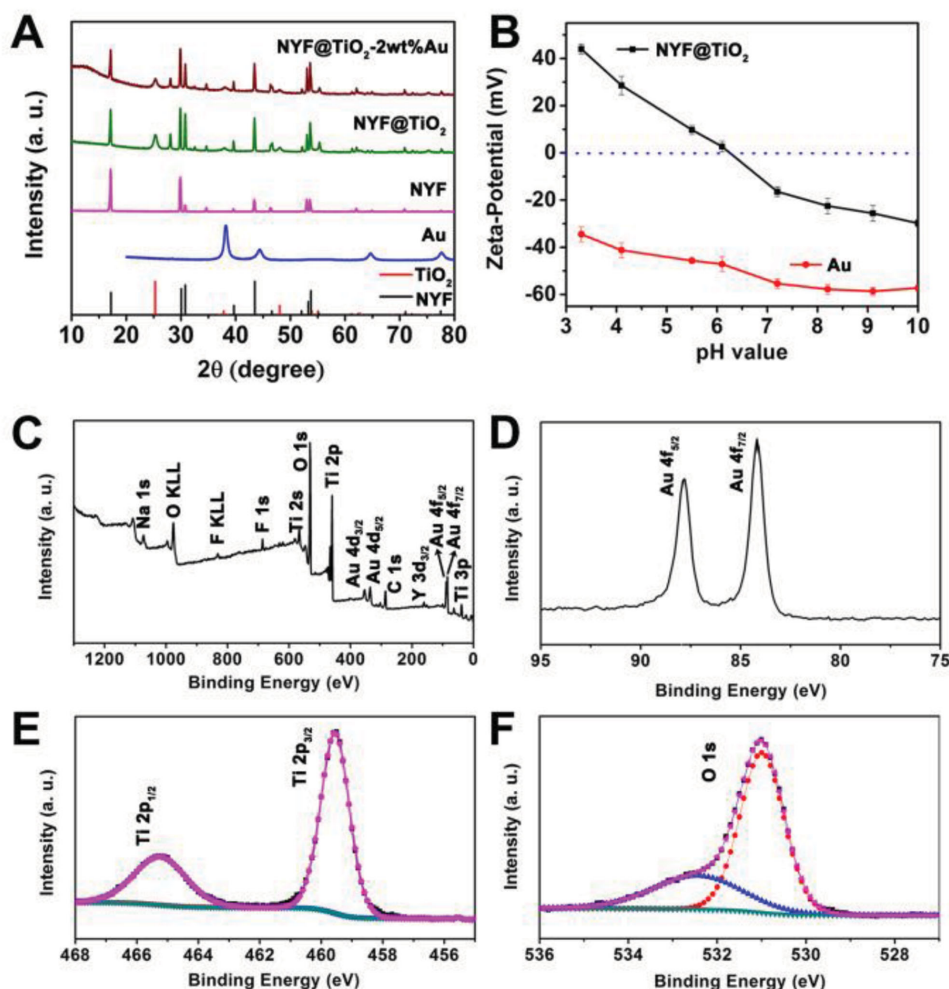
about 900 nm and the shell thickness is about 200 nm. The high-magnification micrograph reveals that the porous shell is made of nanosheets as thin as several nanometers (Figure S3B, Supporting Information). Despite the relatively high growth density, the nanosheets are able to keep free-standing without stacking or agglomeration,[36] which is particularly favorable for easy loading of the Au NPs. Furthermore, these TiO$_2$ nanosheets result in a large surface area so as to enhance their contact with reaction solution for efficient photocatalysis; 4) The Au NP solution was simply mixed with the NYF@TiO$_2$ microspheres and allowed to incubate for 30 min to assemble Au NPs into the porous shell. By controlling Au NP solution volume, we were able to modulate the loading of Au NPs deposited on the surface of porous TiO$_2$ (Figure S4, Supporting Information), the effect of which on photocatalysis will be discussed in later sections.

Hybrid samples containing different amounts of Au NPs were thoroughly characterized by a series of techniques. Herein, as an example, we mainly present the characterization results of the NYF@TiO$_2$ sample loaded with 2 wt% of Au NPs, denoted as NYF@TiO$_2$–2 wt% Au. Figure 1B,C shows the typical transmission electron microscopy (TEM) images of NYF@TiO$_2$–2 wt% Au, confirming the formation of uniform core@shell structured spheres. A high-resolution TEM (HRTEM) image (Figure 1D) clearly demonstrates the attachment of the Au NPs onto the porous TiO$_2$ network. The microstructure was

Materials Views
www.MaterialsViews.com

ADVANCED
FUNCTIONAL
MATERIALS
www.afm-journal.de

FULL PAPER

Figure 2. A) XRD patterns, B) zeta-potential, and XPS spectra of NYF@TiO$_2$–2 wt% Au: C) wide spectrum, D) Au4f, E) Ti2p, and F) O1s.

experimental data very well (Figure S5, Supporting Information). The combination of all these absorption features at different wavelengths in a single architecture allows the broadband photoresponse from UV up to NIR of these hybrid microspheres. The luminescence spectroscopy was further performed in order to testify whether the photon energy generated via the upconversion process by NYF can be transferred to the highly UV-absorbing (also highly catalytically active) TiO$_2$ shell and visible-absorbing Au NPs. As shown in Figure 3B, when NYF is excited by NIR diode laser light (980 nm), it yields two peaks in the UV region at 345 and 361 nm, two blue emission peaks centered at 451 and 477 nm, and two green peaks at 521 and 540 nm. The electronic transitions responsible for these emissions are labeled in Figure 3B. With the TiO$_2$ shell formation, overall the emission intensity is largely enhanced, as straightforwardly observed by eyes. This can be reasonably attributed to the increase of crystallinity of NYF during the calcination treatment at 350 °C. Higher crystallinity of NYF generally means less traps and thus stronger luminescence. Closer examination shows that the intensity ratio of UV-to-blue emission is greatly reduced by three times (0.3 vs 0.1), suggesting the quenching of UV emission due to the absorption of the TiO$_2$ shell. In

other words, this design allows the NIR excitation to "indirectly" excite TiO$_2$, which can then exhibit catalytic activity. Similar quenching, but at different wavelengths, was observed with further decoration of Au NPs. The ratio of integrated intensity of the blue emission band (including peaks centered at 451 and 477 nm) to the green emission band (including emission peaks centered at 521 and 540 nm) significantly increases from 1.8 for NYF@TiO$_2$ to 2.2 for NYF@TiO$_2$–2 wt% Au, suggesting the efficient excitation of the SPR of the Au NPs, again due to the energy transfer from the upconverting core. It was also noticed that the UV emission completely disappears in this case, likely associated with the interband transitions of the Au NPs typically dominating below 400 nm, which are considered not to contribute to photocatalysis in general. Figure 3C shows the results of optical modeling of the emission of the core@shell microspheres. The nanomaterials of the shells (TiO$_2$ nanosheet shell and TiO$_2$–AuNP shell) were modeled as a mixture of the corresponding media using the conventional Maxwell–Garnett approach. In particular, the TiO$_2$ sheets were modeled as a mixture of bulk TiO$_2$ and air, whereas the TiO$_2$–Au NPs composite was modeled as a mixture of bulk TiO$_2$, air and spherical Au NPs. Details of the modeling can be found in the
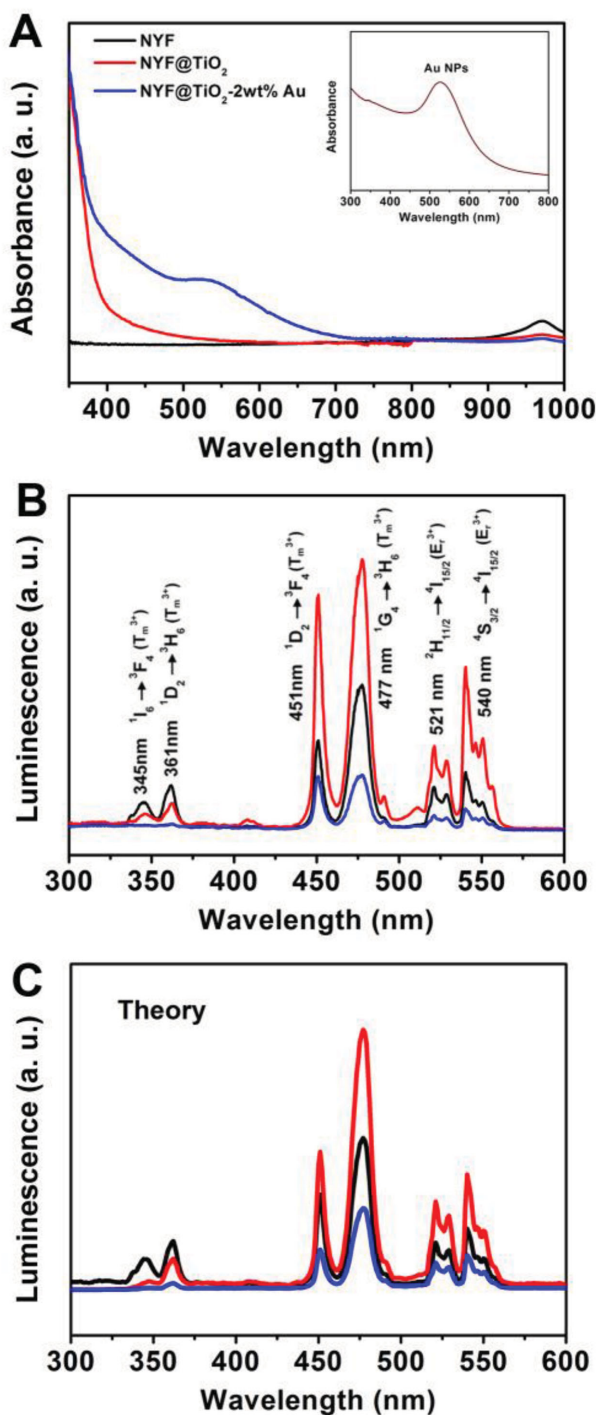
**ADVANCED
FUNCTIONAL
MATERIALS**

www.afm-journal.de

*Materials
Views*

www.MaterialsViews.com

FULL PAPER

Figure 3. A) The UV–vis–NIR absorption spectra, B) upconversion luminescence spectra of NYF, NYF@TiO$_2$, and NYF@TiO$_2$–2 wt% Au, C) theoretical calculations of the luminescence spectra of NYF particles with and without the shell. The inset in A) shows the UV–vis absorption spectrum of Au NPs in solution.

Experimental Section. Then, the experimental emission from the original NYF particles was multiplied by the transmission coefficient of a shell, and good qualitative agreement with the experiment was obtained. This simple calculation confirms our

understanding of the optical properties of the nanocomposite core@shell microspheres used in our experiments. The variation of emission intensities is related to the re-absorption of upconverted emissions by TiO$_2$ and Au NPs, the excitation of which then contributes to photocatalysis.

2.2. Photocatalytic Performance

The photocatalytic activities of samples were investigated by assessing the photodegradation of MO under the separate irradiation of UV, visible, and NIR wavelengths, as well as under simulated solar light (**Figure 4** and Figures S6 and S7, Supporting Information). In order to better understand the mechanisms, the MO degradation process in the presence of NYF@TiO$_2$ samples loaded with varying Au content was monitored and compared with that of the Au NPs, NYF, NYF@TiO$_2$, as well as the benchmark P25 TiO$_2$. It is worth mentioning that the control sample of pure MO solution, without the presence of any samples, does not show any obvious degradation regardless of irradiation wavelengths, excluding the possibility of pure thermal effects on MO degradation. Moreover, no obvious degradation was observed in the presence of Au NPs or NYF, confirming that the hot electrons excited in the Au NPs and excitons in the NYF cores cannot be directly used in the current photocatalytic system and the MO degradation indeed originates from the photocatalysis involving the photocatalyst of TiO$_2$.

Figure 4A shows the UV light irradiation photocatalytic activity of all the samples toward the degradation of MO. After 60 min of UV irradiation, the order of MO degradation can be summarized as follows: NYF@TiO$_2$–1 wt% Au > NYF@TiO$_2$–0.5 wt% Au > Degussa P25 TiO$_2$ > NYF@TiO$_2$ > NYF@TiO$_2$–2 wt% Au > NYF@TiO$_2$–3 wt% Au. In order to understand the MO degradation kinetics in the presence of different samples, ln(C_0/C) data are plotted against reaction time t, where C_0 and C are initial MO concentration and MO concentration at time t, respectively. The linear relationship suggests that the reaction is essentially first order. The reaction rate k was thus estimated from the first-order reaction model shown as follows: ln(C_0/C) = kt.[26] As expected, the order of the reaction rate under UV light irradiation follows the same trend mentioned above (Figure 4F and Figure S7C, Supporting Information). The reaction rate in the presence of NYF@TiO$_2$–1 wt% Au is about 30% higher than that of the benchmark P25. As the SPR of the Au NPs cannot be excited by UV irradiation, the plasmonic effect on photocatalysis can be ruled out in this scenario. The beneficial effect of the Au NPs on the photocatalysis, stemming from the decreased charge recombination in TiO$_2$ due to the electron transfer to the Au NPs,[41] was clearly observed at low Au concentrations. Further increasing Au loading over 1 wt% causes the decrease of the photocatalytic activity, even lower than that of the samples free of the Au NPs.

As for visible photocatalytic activity, it is well known that TiO$_2$ by itself usually is quite poor. The situation changes dramatically with the integration of a small number of Au NPs, since their SPR can be effectively excited by the visible light and excited hot electrons can be transferred to TiO$_2$ to enhance photocatalysis, consistent with previous reports.[41–43]

www.MaterialsViews.com

ADVANCED
FUNCTIONAL
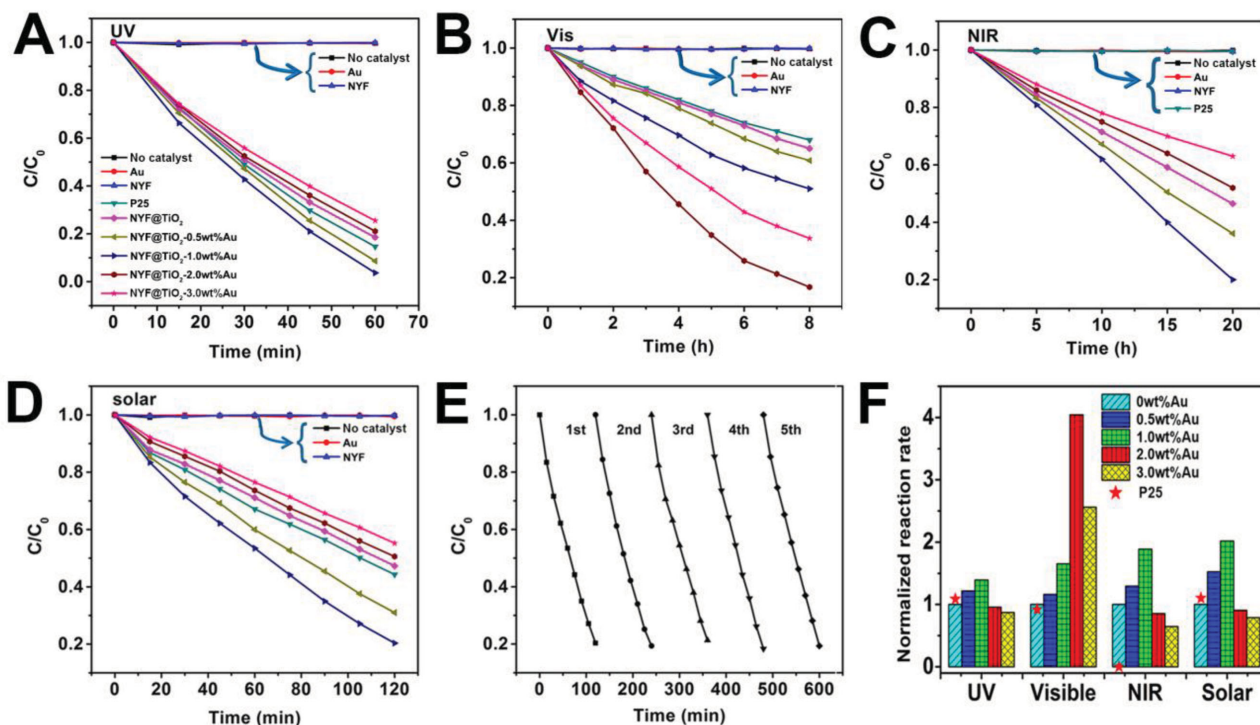MATERIALS
www.afm-journal.de

FULL PAPER

Figure 4. Photocatalytic degradation of MO aqueous solution in the presence of various samples under A) UV, B) visible, C) NIR, and D) simulated sunlight irradiation. E) Photocatalytic degradation of MO aqueous solution in the presence of NYF@TiO$_2$–1 wt% Au under simulated sunlight irradiation from the first to fifth cycles. F) Comparison of normalized photocatalytic degradation rate of MO in the presence of the NYF@TiO$_2$ core@shell samples loaded with varying Au content from 0 to 3 wt% under UV, visible, NIR, and simulated sunlight irradiation. For the purpose of comparison, all the reaction rate data are normalized to those of NYF@TiO$_2$–0 wt% Au. The data of the benchmark of P25 TiO$_2$ are also included for comparison.

The highest activity was observed at the 2 wt% of Au loading (Figure 4F and Figure S7A,D, Supporting Information), with the reaction rate being ≈4.5 times that of the benchmark P25. Although the reaction rate decreases when the Au loading exceeds 2 wt%, it is still higher than that of the samples with no Au loading (including P25). Such observations imply that exact enhancement mechanisms and related factors to consider with the introduction of Au NPs are different in this case with respect to those under UV irradiation. It should be noted that very limited visible photoactivity of pure P25 TiO$_2$ has been attributed to the presence of defect states.[44]

As both TiO$_2$ and Au NPs do not absorb in the NIR range, no NIR photoactivity is anticipated for the systems involving only coupled TiO$_2$ and Au components. NYF has been widely recognized as one of the most efficient hosts for upconversion.[45] By appropriately selecting dopant ions, upconverted emission at desired wavelengths can be achieved. In the current work, NaYF$_4$:Yb^{3+}, Er^{3+}, Tm^{3+}, which can show upconverted emissions in the UV range and at wavelengths overlapping with the Au SPR band in the visible range, is integrated with TiO$_2$ and Au NPs as the core for the purpose of efficiently using the absorbed NIR energy in photocatalysis through energy transfer among nanocomponents. As shown in Figure 4C, the photodegradation was clearly observed for NYF@TiO$_2$. Loading of the Au NPs further enhances the NIR activity, with the maximum achieved at 1 wt% of the Au NPs. More loading simply leads to the decrease of the catalytic efficiency (Figure 4F and Figure S7E, Supporting Information). Although the NIR photoactivity is

much lower than that under UV and visible illumination, the combination effect of NYF, TiO$_2$, and Au components on NIR photocatalysis is considerable, and has not been previously studied.

Toward practical applications, we further checked the photocatalytic property of the above hybrid photocatalysts under simulated solar light irradiation. To this end, a 150 W solar simulator was used as the light source. NYF@TiO$_2$–1 wt% Au leads to the maximum degradation rate, nearly two times that of the benchmark P25 TiO$_2$ (Figure 4D,F and Figure S7B,F, Supporting Information). Furthermore, for practical photocatalytic applications, the reusability of the photocatalyst systems is an important but tough task due to the leakage of involved active components and materials during photocatalysis. Interestingly, all the NYF@TiO$_2$–Au materials investigated herein exhibit very stable photocatalytic performance under UV, visible, NIR, and simulated solar light irradiation (Figure 4E and Figure S6, Supporting Information). No obvious reduction in the photocatalytic efficiency was observed even after five cycles, strongly suggesting their great potential for practically viable, high-efficiency, and stable photocatalysts.

In order to better understand the photocatalytic process, the active species generated during the photocatalysis with the presence of the NYF@TiO$_2$–1 wt% Au under simulated solar light irradiation were identified by free radical and hole trapping experiments. Specifically, *tert*-butyl alcohol (*t*-BuOH), disodium ethylenediaminetetraacetate (Na$_2$EDTA), and 1,4-benzoquinone (BQ) were used as hydroxyl radical (OH·), hole, and

**ADVANCED
FUNCTIONAL
MATERIALS**

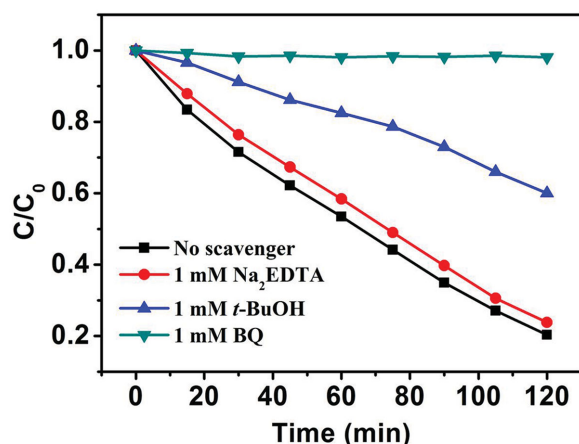www.afm-journal.de

FULL PAPER

www.MaterialsViews.com

Figure 5. Photocatalytic degradation of MO aqueous solution in the presence of NYF@TiO₂–1 wt% Au and different scavengers under simulated solar light irradiation.

superoxide radical ($O_2^{-•}$) scavengers, respectively.[46] **Figure 5** shows the influence of various scavengers on the photocatalytic activity of NYF@TiO₂–1 wt% Au toward the degradation of MO. Compared with the scavenger-free system, the presence of the hole scavenger Na₂EDTA (1×10^{-3} M) has only slight effect on the photocatalytic activity and the MO degradation remains almost unaffected. In clear contrast, when the superoxide radical ($O_2^{-•}$) scavenger BQ is added to the reaction system, the photodegradation is greatly restrained compared to the reaction without this radical scavenger and indeed, no obvious MO degradation was observed. The photocatalytic activity is also considerably reduced when hydroxyl radical ($OH^•$) scavenger t-BuOH is introduced to the reaction system. At 120 min, ≈40% of MO is photodegraded, about half of what (≈80%) can be achieved when it is absent. These results strongly suggest that superoxide radical ($O_2^{-•}$) and hydroxyl radical ($OH^•$) are the main active species for this photocatalytic reaction.

2.3. Discussion

Based on the above results, it is clear that we have rationally designed and realized a hybrid structure in order to obtain broadband photocatalysts by taking advantages of both plasmon and upconversion effects. Specifically, the hybrid structure is composed of UV-absorbing, catalytically active TiO₂, visible-absorbing plasmonic Au, and NIR-absorbing upconverting NYF components, organized in a core@porous-shell structure. As mentioned above, SPR can, in general, enhance photocatalysis via SPR induced hot electron transfer, enhancement in the local electromagnetic field (and thereby enhanced exciton generation rate), and increase in light scattering (and thus increased photon path length).[10,11,16] The exact enhancement mechanism relies on geometrical features and optical properties as well. For instance, for the optical properties, the near field electromagnetic mechanism requires the spectral overlap between SPR and semiconductor absorption.[47] Likewise, the scattering mechanism only works when SPR energy is larger or at least equal to the bandgap of a semiconductor.[48] As

such, both mechanisms are expected not to be efficient in the coupled Au–TiO₂ system, since TiO₂ does not efficiently absorb at SPR wavelengths. Instead, the hot electron transfer appears viable and most attractive for this specific system. In order to maximize the SPR induced electron transfer, close contact and large interfacial area between Au and TiO₂ are extremely important. Bearing this in mind, we used "bare," 5 nm (in diameter) Au NPs, which can have intimate contact with TiO₂. At this size, the absorption, instead of scattering, is dominant, which favors the electron transfer. Moreover, as compared with larger Au particles, the use of these small ones allows higher interfacial area when the identical weight of Au is loaded. Additionally, the ultrathin 2D sheet-like porous TiO₂ network favors NP loading, not only on the external surface like that in the case of a compact shell, but also inside the shell, to enlarge the Au/TiO₂ interface, as well as TiO₂/solution contact. Because the charge separation now takes place throughout the TiO₂ shell in contact with reaction solution, charge recombination is also largely reduced. The inside loading of Au NPs also allows some of them to be in the vicinity of the NYF core, preferred for energy transfer. In short, the structure is designed in such a way to enable the efficient charge or energy transfer between the nanocomponents, as well as reduce the probability of electron–hole recombination. The ultimate purpose is to maximize all the beneficial interactions.

Based on the structural features and experimental results of catalysis, the enhanced, excellent photocatalytic activity of NYF@TiO₂–Au under UV, visible, and NIR light irradiation could be ascribed to different mechanisms (**Figure 6**). Upon exposure to the UV light (Figure 6A), a significant number of reductive electrons and highly oxidative holes are generated by band gap excitation of TiO₂. Then, the excited electrons can be transferred from the CB of TiO₂ to the Au NPs. This process helps to minimize the electron–hole recombination, and the transferred electrons can react with the adsorbed O₂ on the Au surface to form superoxide anion radicals ($O_2^{-•}$).[42] Such beneficial charge transfer behavior has previously been reported,[43] which however has nothing to do with their plasmonic effect. Simultaneously, the holes remaining in the TiO₂ shell can directly attack MO molecules or be used for the generation of $OH^•$ radicals. Although both $O_2^{-•}$ and $OH^•$ radicals have been considered as reactive species, based on the scavenger measurements the role of $O_2^{-•}$ is much more significant in the degradation of MO molecules. Therefore, the Au NP deposition on the surface of the porous TiO₂ shells can enhance the photocatalytic efficiency under UV light, despite the absence of the SPR excitation. However, the positive effect is limited to a very small quantity. At a relatively higher Au concentration, the activity reduces instead. As seen in Figure 4F, the optimal Au loading is 1 wt%, where the sample exhibits the highest photocatalytic activity under UV irradiation. It has been documented that there is a trade-off of "active" surface area of TiO₂ with metal loading.[49,50] In addition, the number of "useful" photons (UV for TiO₂) reaching the TiO₂ surface is decreased due to the Au surface coverage and its interband absorption. The defects at the Au/TiO₂ interface can also create new recombination pathways to accelerate charge carrier recombination.[24,41] The 1 wt% of optimal Au loading is determined by the competition of all these beneficial and adverse factors closely associated with the Au NP introduction.
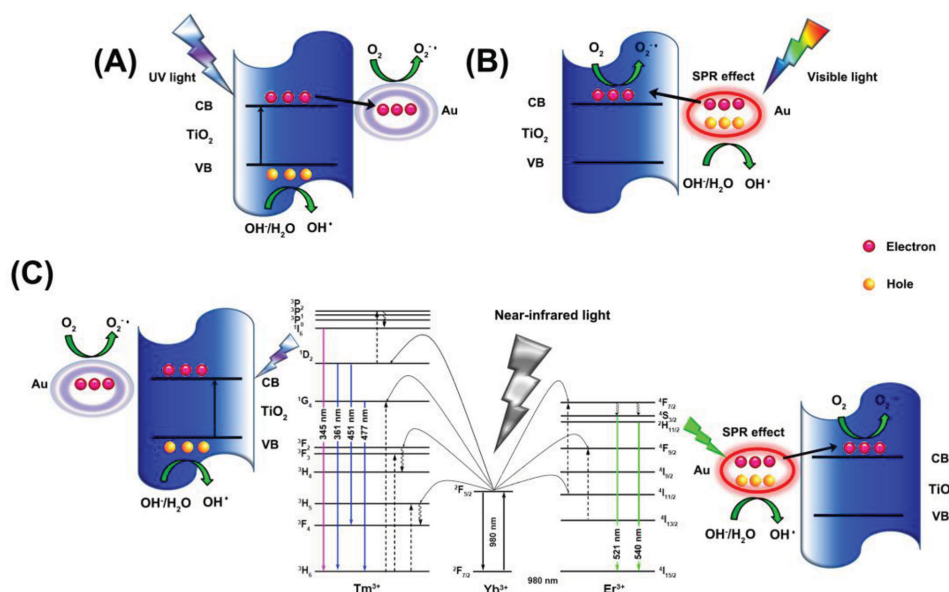
www.MaterialsViews.com

ADVANCED
FUNCTIONAL
MATERIALS
www.afm-journal.de

FULL PAPER

Figure 6. A schematic illustration of the photocatalysis mechanisms under A) UV, B) visible, and C) NIR irradiation, respectively.

NYF@TiO$_2$–Au can also interact with visible light through the excitation of Au SPR, and thus showing visible photoactivity. The excited SPR induces the efficient injection of hot electrons from the Au NPs to TiO$_2$ (Figure 6B), which is opposite to what happens under UV illumination. Such electrons injected into the CB of the TiO$_2$ can enhance the generation of active O$_2^{-\bullet}$ radicals on the TiO$_2$ surface, playing a dominant role in MO degradation as evidenced by the scavenger measurements. On the other hand, the holes retained in the Au NPs can be used for the generation of active OH$^\bullet$ radicals,[42] which can also contribute to the degradation of MO. As the visible light absorption and subsequently hot electron injection are expected to be directly related to the number of Au NPs on the TiO$_2$ surface, it is expected that higher loading of Au NPs would lead to higher visible photoactivity. But, herein, the optimal loading of the Au NPs was once again observed, but at the content twice that under UV illumination. As shown in Figure 4F, further increase in Au content over 2 wt% leads to the decrease of photocatalytic activity. This deterioration of the catalytic performance can be primarily explained by the introduction of interface trap states between the metal and semiconductor, which accelerate the electron–hole recombination.[51] But, overall, the positive contribution of the Au NPs overrides; all the Au-involved samples show appreciably higher visible activity than Au-free samples (Figure 4B).

Figure 6C further illustrates the mechanism for NIR-driven photocatalysis. First, the 980 nm irradiation excites Yb^{3+} ions because of their relatively larger absorption cross section than Tm^{3+} and Er^{3+} ions, resulting in the population of the long-lived $^2F_{5/2}$ level in Yb^{3+}. Then, the Tm^{3+} and Er^{3+} ions can be excited indirectly due to the efficient energy transfer from Yb^{3+}. The UV and blue emissions, centered at 345, 361, 451, 477 nm, are then attributed to the transitions of $^1I_6 \rightarrow ^3F_4$, $^1D_2 \rightarrow ^3H_6$, $^1D_2 \rightarrow ^3F_4$, and $^1G_4 \rightarrow ^3H_6$ of Tm^{3+}, respectively. For the green emission, peaks centered at 521 and 540 nm, which overlap with the SPR band of the Au NPs, are assigned to the transitions

of $^2H_{11/2} \rightarrow ^4I_{15/2}$ and $^4S_{3/2} \rightarrow ^4I_{15/2}$ of Er^{3+}, respectively. The upconverted UV emission from the NYF core can be efficiently absorbed by the TiO$_2$ shell closely surrounding the core, as evidenced by the experimental and theoretical luminescence investigations (Figure 3B,C). Such energy transfer can then produce electron/hole pairs in the TiO$_2$, same as under UV illumination, which can subsequently participate in catalytic reactions. At the same time, the upconverted green emission from the NYF core can be absorbed by nearby Au NPs to excite their SPR. Then following the same pathway described for the visible illumination, charge separation in the Au NPs takes place by transferring photoinduced hot electrons from the Au NPs to the CB of TiO$_2$. As a result, both the energy transfer to nearby TiO$_2$ and Au NPs from the upconverting cores helps to improve the NIR photocatalytic activity. Same as under the UV irradiation, the sample loaded with 1wt% of Au NPs exhibits the highest photocatalytic activity under NIR irradiation. It seems that NIR catalytic behavior somewhat follows the trend of UV behavior (Figure 4F). Quite likely, the contribution to the NIR photocatalysis arising from the energy transfer from the NYF core to the TiO$_2$ shell is larger than that of the energy transfer to the Au NPs. Our deduction is further confirmed by carefully comparing the behavior of NYF, NYF@TiO$_2$, and NYF@TiO$_2$–1 wt% Au. The MO degradation increases from 0% to 53% with the deposition of TiO$_2$, and further to 75% with Au integration at 1 wt% (Figure 4C). Although both processes are playing a role in enabling the NIR photocatalysis, the contribution of the NYF-to-TiO$_2$ energy transfer doubles that of the NYF-to-Au energy transfer. Next step performance optimization may be deployed by further improving the upconverted UV emission through suitably tuning the doping of the NYF core. Under the simulated solar light, all above mentioned processes can actually take place. The observed photoactivity is the consequence of the interplay of all of them, eventually leading to considerably higher activity than the benchmark photocatalyst of P25 TiO$_2$.

3. Conclusions

In summary, we have combined the concepts of plasmonics and upconversion into our design of broadband photocatalysts. A facile approach has been developed for the synthesis of the nanostructured architecture of Au-loaded, NYF@TiO₂ core@porous-shell microspheres. The structure was designed in such a way to favor the efficient electron or energy transfer among constituent components by taking into consideration multiple factors with the purpose to greatly benefit from plasmon and upconversion effects. The synthesized NYF@TiO₂–Au microspheres are able to capture photons over a wide wavelength range from UV, visible, to NIR, and show excellent photocatalytic activity, significantly superior to the benchmark photocatalyst of P25 TiO₂. Based on photocatalysis studies under separate UV, visible, and NIR excitations and with varying Au loading, different involved mechanisms and relevant factors are discussed in detail. Theoretical calculations further support our interpretations of the catalytic mechanisms. Last, but not least, the NYF@TiO₂–Au photocatalysts show very good structural stability and reusability, suggesting their high potential as high-efficiency catalysts. The work represents the first demonstration of combining both plasmonic and upconversion nanocomponents with porous TiO₂ into a single system for creating a broadband, high-efficiency nanohybrid photocatalyst.

4. Experimental Section

Preparation of Au NPs: Laser ablation was carried out with a KrF excimer laser (GSI Lumonics PM-846, wavelength: 248 nm, repetition rate 20 Hz). The beam was focused by an objective lens, with a focal length of 7.5 cm, onto a gold plate with a diameter of 8 mm and the thickness of 1.5 mm. The gold target was placed at the bottom of a 6 mL glass vessel filled with pure water (pH ≈ 6.5). The depth of the water layer above the target was ≈10 mm. Laser influence on the target was set at ≈40.0 J cm^{-2} during all ablation processes. The concentration of as-prepared Au NPs in solution is 30 ppm based on neutron activation analysis (NAA) characterization.

Preparation of NYF Microspheres: In a typical synthesis, 1.488 mL of Y(NO₃)₃ (0.5 M), 0.5 mL of Yb(NO₃)₃ (0.5 M), 0.1 mL of Er(NO₃)₃ (0.01 M), and 0.5 mL of Tm(NO₃)₃ (0.01 M) stock solutions were added to 15 mL of aqueous solution containing 0.5 mmol of trisodium citrate (labeled as Cit^{3-}) and magnetically stirred for 1 h, forming the lanthanide (Ln^{3+})–Cit^{3-} complex. Then, 4 mmol of NaF and 20 mmol of urea were introduced into the solution and the mixture solution was further stirred for 1 h before it was transferred into a Teflon bottle held in a stainless steel autoclave, and maintained at 180 °C for 12 h. As the autoclave cooled to room temperature naturally, the precipitates were separated by centrifugation, washed with ethanol and deionized water in sequence, and then dried in air at 80 °C for 12 h.

Preparation of NYF@TiO₂ Core@Porous-Shell Microspheres: The NYF microspheres (0.05 g) were dispersed in isopropanol (42.00 mL), followed by the addition of diethylenetriamine (DETA) (0.04 mL). After stirring for 10 min, titanium isopropoxide (97%) (2 mL) was added to the solution. The mixture was then transferred into a Teflon bottle held in a stainless steel autoclave with a capacity of 100 mL and kept at 200 °C for 24 h. As the autoclave cooled to room temperature naturally, the precipitates were separated by centrifugation, washed with ethanol, and then dried in air at 80 °C for 12 h. Finally, the product was calcined at 350 °C for 2 h with a heating rate of 1 °C min^{-1} to obtain the high crystalline phases of NYF and anatase TiO₂.

Preparation of Au NPs Decorated NYF@TiO₂ Core@Porous-Shell Microspheres: To 10 mg of NYF@TiO₂ core@shell microspheres, a certain amount of freshly prepared Au NP solution was added and mixed by shaking. The mixture solution was incubated at room temperature for 30 min. After this, the pink precipitate was recovered by centrifugation, followed by washing with ethanol and deionized water in sequence, and then dried in air at 60 °C for 12 h. In this work, various volumes of freshly prepared Au NP solution were employed to prepare Au-decorated NYF@TiO₂ core@shell microspheres with varying Au NP contents. The Au NPs were successfully loaded into TiO₂ network at the content of 0.5, 1.0, 2.0, and 3.0 wt% and corresponding hybrid samples are labeled as NYF@TiO₂–0.5 wt% Au, NYF@TiO₂–1.0 wt% Au, NYF@TiO₂–2.0 wt% Au, and NYF@TiO₂–3.0 wt% Au, respectively.

The Evaluation of Photocatalytic Activity: The photocatalytic activity of the NYF@TiO₂–Au core@shell microspheres was investigated by monitoring the photodegradation of methyl orange (MO). In a typical measurement, 10 mg of the NYF@TiO₂–Au core@shell microspheres were added to 10 mL of MO solution (20 mg L^{-1}) in a 100 mL quartz flask. Prior to photoirradiation, the suspension was magnetically stirred in the dark for 0.5 h to establish adsorption–desorption equilibrium between the MO and the surface of the catalysts under ambient conditions. A commercial photoreactor (LUZ-4V, Luzchem) equipped with fourteen 8 W ultraviolet (Luzchem LZC-UVA) lamps was used for UV photocatalysis experiments. Visible light photocatalytic reactions were performed by using a 300 W xenon lamp (optical filter, $\lambda > 420$ nm) as an irradiation source. A cooling water circulator, which is made of quartz, was installed between the light and quartz flask reactor to keep the reaction temperature constant. A 2 W 980 nm diode laser was used as the NIR light source. A 150 W solar simulator was used as the simulated solar light source. At varied irradiation time intervals, an aliquot of the mixed solution was collected and centrifuged, and the residual concentration of MO in the supernatant was analyzed by UV–vis absorption spectrometry. To evaluate the photocatalytic stability of the NYF@TiO₂–Au core@shell microspheres, MO photocatalytic degradation testing was repeated five times in the presence of the NYF@TiO₂–Au core@shell microspheres. After each degradation cycle, the degraded solution was centrifuged. The obtained precipitate was washed with pure water for several times to get the clean photocatalyst, which was then dried at 60 °C for the next degradation cycle. In order to identify the active species generated in the photocatalytic process, *tert*-butyl alcohol (*t*-BuOH), disodium ethylenediaminetetraacetate (Na₂EDTA), and 1,4-benzoquinone (BQ) were used as hydroxyl radical (OH·), hole and superoxide radical (O₂·$^{-}$) scavengers, respectively. The trapping experiment was done in the same way as the photodegradation tests, except for the introduction of scavengers.

Characterization: A transmission electron microscope (TEM, JEOL 2100F), equipped with an energy-dispersive X-ray (EDX) spectrometer, was applied for the analysis of microstructure and composition. TEM and EDX samples were prepared by depositing one or two droplets of the colloidal suspension in hexane onto copper grids coated with thin carbon film. Powder X-ray diffraction (XRD) of Au NPs was performed on a Philips X'pert diffractometer using a Cu Kα radiation source ($\lambda = 0.154$ nm). The crystal structure of other samples was characterized by a Bruker D8 Advanced Diffractometer, again using Cu Kα radiation. The chemical states of involved elements were studied using X-ray photoelectron spectroscopy (XPS, ESCALAB 220I-XL spectrometer) equipped with an Al Kα (1486.6 eV) monochromatic source. Binding energies of various peaks were calibrated using the binding energy of C1s (284.6 eV). UV–vis-NIR absorption spectroscopy was conducted using a Varian 5000 spectrometer. Neutron activation analysis was performed using a SLOWPOKE nuclear reactor to quantify the concentration of Au NPs in solution, as well as the content of Ti and Au in NYF@TiO₂–Au. Zeta-potential measurements were performed with a Brookhaven ZETAPALS Analyzer for colloidal samples (1.5 mL) at different pH values in standard 10 mm all-side-transparent PMMA cuvettes. Upconversion luminescence measurements were carried out under 975 nm excitation using a Thorlabs fiber-coupled laser diode (maximum power 330 mW) focused on the sample using a lens to obtain a spot with Gaussian

www.MaterialsViews.com

ADVANCED
FUNCTIONAL
MATERIALS
www.afm-journal.de

FULL PAPER

intensity distribution (0.4 mm in diameter). Emission light was collected by a lens in a 90° configuration, and then transferred using an optical fiber to a spectrophotometer (Avaspec-2048L-USB2). All the emission spectra were corrected by the instrument response curve, which has been calibrated using an Ocean Optics halogen tungsten lamp. All experiments were carried out under ambient conditions.

Theoretical Modeling of the Shell Nanomaterials: First, we look at the optical properties of the shell materials. In the case of fuzzy TiO_2 shell, we can model its dielectric function as a mixture of bulk TiO_2 and air. Using the Maxwell–Garnett formula,[52] we get the effective dielectric function of TiO_2–air in the form

$$\varepsilon_{\mathrm{eff},TiO_2-\mathrm{air}}(\lambda) = \frac{\varepsilon_{TiO_2}(1+2f_{TiO_2}) + \varepsilon_0(2f_{TiO_2}-2)}{\varepsilon_{TiO_2}(1-f_{TiO_2}) + \varepsilon_0(2+f_{TiO_2})}$$

where $\varepsilon_{TiO_2}(\lambda)$ is the dielectric function of bulk TiO_2 taken from the tables in ref. [52] and the matrix dielectric constant $\varepsilon_0 = 1$ (air). The parameter f_{TiO_2} is the bulk filling factor of TiO_2. The case of TiO_2–air–AuNP composite can be considered as a mixture of TiO_2–air and spherical Au particles. Then, we get

$$\varepsilon_{\mathrm{eff},TiO_2-\mathrm{air\text{-}AuNPs}}(\lambda) = \frac{\varepsilon_{Au}(1+2f_{AuNP}) + \varepsilon_{TiO_2}(2f_{AuNP}-2)}{\varepsilon_{Au}(1-f_{AuNP}) + \varepsilon_{TiO_2}(2+f_{AuNP})}$$

where f_{AuNP} is the Au filling factor and ε_{Au} is the bulk dielectric constant of gold.[53] The emission from the central NYF particle can be modeled in the following way. The core-shell microspheres are relatively large and, in the first approximation, the shells can be considered as films. Then, the optical transmission coefficients of such films can be estimated as

$$T_{TiO_2-\mathrm{air}}(\lambda) = e^{-\alpha_{TiO_2-\mathrm{air}} \cdot d_{\mathrm{shell}}}$$

$$T_{TiO_2\text{-air}-\mathrm{AuNPs}}(\lambda) = e^{-\alpha_{TiO_2\text{-air}\cdot\mathrm{AuNPs}} \cdot d_{\mathrm{shell}}}$$

where $\alpha_{TiO_2-\mathrm{air}}$ and $\alpha_{TiO_2\text{-air-AuNPs}}$ are the corresponding bulk absorption coefficients and d_{shell} is the shell thickness. The absorption coefficients are expressed via the effective dielectric constants

$$\alpha_{TiO_2-\mathrm{air}} = \frac{4\pi}{\lambda} \mathrm{Im}\sqrt{\varepsilon_{\mathrm{eff},TiO_2-\mathrm{air}}}$$

$$\alpha_{TiO_2-\mathrm{air}-\mathrm{AuNPs}} = \frac{4\pi}{\lambda} \mathrm{Im}\sqrt{\varepsilon_{\mathrm{eff},TiO_2-\mathrm{air}-\mathrm{AuNPs}}}$$

In the next step, we estimate the modification of the emissions using the known emission of NYF particles without a shell, $I_{NYF}(\lambda)$, taken from the experiment. Then, the emissions of the core-shell microspheres are given by

$$I_{NYF\text{-}TiO_2-\mathrm{air}}(\lambda) = I_{NYF}(\lambda) \cdot T_{TiO_2-\mathrm{air}}(\lambda) = I_{NYF}(\lambda) \cdot e^{-\alpha_{TiO_2-\mathrm{air}} \cdot d_{\mathrm{shell}}}$$

$$I_{NYF\text{-}TiO_2-\mathrm{air}-\mathrm{AuNPs}}(\lambda) = I_{NYF}(\lambda) \cdot T_{TiO_2-\mathrm{air\text{-}AuNPs}}(\lambda) = I_{NYF}(\lambda) \cdot e^{-\alpha_{TiO_2-\mathrm{air\text{-}AuNPs}} \cdot d_{\mathrm{shell}}}$$

Now, we will use the parameters of our shells taken from the experiment. The shell thickness is 200 nm and the 5 nm AuNP filling factor can be estimated $f_{AuNP} = 0.065$. The filling factor of TiO_2 is a fitting parameter. We can get it by looking at the position of experimental plasmon peak, that is, ≈550 nm. Then, if we take $f_{TiO_2} = 0.5$, we obtain good agreement for the plasmon-peak position. Figure S5, Supporting Information, shows the results for the calculated absorption coefficients. Since we have available only the bulk data for the dielectric constant for TiO_2, we shift a little bit the band edge in the corresponding function $\varepsilon_{TiO_2}(\lambda)$. This is to get agreement with the experimental absorption of TiO_2-NYF NPs where the band edge of TiO_2 is shifted to the red since we deal with TiO_2 in the form of nanosheets. After using the above approximations and overall realistic parameters, we arrive at the results shown in

Figure 3C. As we can see, our calculations reproduce the experimental emissions well. It confirms our understanding of the optical interactions of the nanoelements in our structures.

Supporting Information

Supporting Information is available from the Wiley Online Library or from the author.

Acknowledgements

[1] S. H. Joo, J. Y. Park, C. K. Tsung, Y. Yamada, P. D. Yang, G. A. Somorjai, *Nat. Mater.* **2009**, *8*, 126.

[2] Z. H. Xu, P. A. Ma, C. X. Li, Z. Y. Hou, X. F. Zhai, S. S. Huang, J. Lin, *Biomaterials* **2011**, *32*, 4161.

[3] R. G. Chaudhuri, S. Paria, *Chem. Rev.* **2012**, *112*, 2373.

[4] W. Li, D. Y. Zhao, *Adv. Mater.* **2013**, *25*, 142.

[5] a) J. Tang, Z. Huo, S. Brittman, H. Gao, P. Yang, *Nat. Nanotechnol.* **2011**, *6*, 568; b) W. Zhou, T. Li, J. Wang, Y. Qu, K. Pan, Y. Xie, G. Tian, L. Wang, Z. Ren, B. Jiang, H. Fu, *Nano Res.* **2014**, *7*, 731; c) W. J. Ong, L. L. Tan, S. P. Chai, S. T. Yong, A. R. Mohamed, *Nano Res.* **2014**, *7*, 1528.

[6] a) W. Li, Y. H Deng, Z. X Wu, X. F. Qian, J. P. Yang, Y. Wang, D. Gu, F. Zhang, B. Tu, D. Y. Zhao, *J. Am. Chem. Soc.* **2011**, *133*, 15830; b) S. Park, D. Kim, C. W. Lee, S. D. Seo, H. J. Kim, H. S. Han, K. S. Hong, D. W. Kim, *Nano Res.* **2014**, *7*, 144.

[7] C. Chen, W. Ma, J. Zhao, *Chem. Soc. Rev.* **2010**, *39*, 4206.

[8] Y. C. Pu, G. M. Wang, K. D. Chang, Y. C. Ling, Y. K. Lin, B. C. Fitzmorris, C. M. Liu, X. H. Lu, Y. X. Tong, J. Z. Zhang, Y. J. Hsu, Y. Li, *Nano Lett.* **2013**, *13*, 3817.

[9] X. Feng, K. Zhu, A. J. Frank, C. A. Grimes, T. E. Mallouk, *Angew. Chem. Int. Ed.* **2012**, *51*, 2727.

[10] J. Li, S. K. Cushing, P. Zheng, D. Chu, N. Wu, *Nat. Commun.* **2013**, *4*, 2651.

[11] S. K. Cushing, J. T. Li, F. K. Meng, T. R. Senty, S. Suri, M. J. Zhi, M. Li, A. D. Bristow, N. Q. Wu, *J. Am. Chem. Soc.* **2012**, *134*, 15033.

[12] R. Asahi, T. Morikawa, T. Ohwaki, K. Aoki, Y. Taga, *Science* **2001**, *293*, 269.

[13] W. Zhao, Y. Sun, F. N. Castellano, *J. Am. Chem. Soc.* **2008**, *130*, 12566.

[14] H. Tada, Q. L. Jin, H. Nishijima, H. Yamamoto, M. Fujishima, S. I. Okuoka, T. Hattori, Y. Sumida, H. Kobayashi, *Angew. Chem. Int. Ed.* **2011**, *50*, 3501.

[15] L. Liu, S. Ouyang, J. Ye, *Angew. Chem. Int. Ed.* **2013**, *52*, 6689.

[16] S. Linic, P. Christopher, D. B. Ingram, *Nat. Mater.* **2011**, *10*, 911.

[17] W. B. Hou, S. B. Cronin, *Adv. Funct. Mater.* **2013**, *23*, 1612.

[18] Y. Tian, T. Tatsuma, *J. Am. Chem. Soc.* **2005**, *127*, 7632.

[19] H. Li, Z. Bian, J. Zhu, Y. Huo, H. Li, Y. Lu, *J. Am. Chem. Soc.* **2007**, *129*, 4538.

[20] W. H. Hung, M. Aykol, D. Valley, W. Hou, S. B. Cronin, *Nano Lett.* **2010**, *10*, 1314.

[21] P. Christopher, H. Xin, S. Linic, *Nat. Chem.* **2011**, *3*, 467.

FULL PAPER

[22] J. Lee, S. Mubeen, X. Ji, G. D. Stucky, M. Moskovits, *Nano Lett.* **2012**, *12*, 5014.

[23] S. T. Kochuveedu, Y. H. Jang, D. H. Kim, *Chem. Soc. Rev.* **2013**, *42*, 8467.

[24] Z. Bian, T. Tachikawa, P. Zhang, M. Fujitsuka, T. Majima, *J. Am. Chem. Soc.* **2014**, *136*, 458.

[25] M. Jakob, H. Levanon, *Nano Lett.* **2003**, *3*, 353.

[26] J. Zhang, G. Chen, M. Chaker, F. Roser, D. Ma, *Appl. Catal. B: Environ.* **2013**, *132*, 107.

[27] J. Zhang, D. Han, H. Zhang, M. Chaker, Y. Zhao, D. Ma, *Chem. Commun.* **2012**, *48*, 11510.

[28] W. Qin, D. Zhang, D. Zhao, L. Wang, K. Zheng, *Chem. Commun.* **2010**, *46*, 2304.

[29] Z. X. Li, F. B. Shi, T. Zhang, H. S. Wu, L. D. Sun, C. H. Yan, *Chem. Commun.* **2011**, *47*, 8109.

[30] Y. Tang, W. Di, X. Zhai, R. Yang, W. Qin, *ACS Catal.* **2013**, *3*, 405.

[31] C. K. Chen, H. M. Chen, C. J. Chen, R. S. Liu, *Chem. Commun.* **2013**, *49*, 7917.

[32] X. Wu, S. Yin, Q. Dong, B. Liu, Y. Wang, T. Sekino, S. W. Lee, T. Sato, *Sci. Rep.* **2013**, *3*, 2918.

[33] W. K. Su, M. M. Zheng, L. Li, K. Wang, R. Qiao, Y. J. Zhong, Y. Hua, Z. Q. Li, *J. Mater. Chem. A*, **2014**, *2*, 13486.

[34] R. Lv, S. Gai, Y. Dai, N. Niu, F. He, P. Yang, *ACS Appl. Mater. Interfaces* **2013**, *5*, 10806.

[35] J. S. Chen, Y. L. Tan, C. M. Li, Y. L. Cheah, D. Y. Luan, S. Madhavi, F. Y. C. Boey, L. A. Archer, X. W. Lou, *J. Am. Chem. Soc.* **2010**, *132*, 6124.

[36] H. B. Wu, A. Pan, H. H. Hng, X. W. Lou, *Adv. Funct. Mater.* **2013**, *23*, 5669.

[37] J. Zhang, D. Riabinina, M. Chaker, D. Ma, *Langmuir* **2012**, *28*, 2858.

[38] V. B. Crist, *PDF Handbooks of Monochromatic XPS Spectra.* The Elements and Native Oxides, Vol. *1*: International, LLC, CA, USA **1999**.

[39] S. Naya, T. Niwa, T. Kume, H. Tada, *Angew. Chem. Int. Ed.* **2014**, *53*, 7305.

[40] X. Chen, L. Liu, P. Y. Yu, S. S. Mao, *Science* **2011**, *331*, 746.

[41] C. G. Silva, R. Juárez, T. Marino, R. Molinari, H. García, *J. Am. Chem. Soc.* **2011**, *133*, 595.

[42] S. Linic, P. Christopher, H. Xin, A. Marimuthu, *Acc. Chem. Res.* **2013**, *46*, 1890.

[43] P. V. Kamat, *J. Phys. Chem. B* **2002**, *106*, 7729.

[44] J. Yang, D. Wang, H. Han, C. Li, *Acc. Chem. Res.* **2013**, *46*, 1900.

[45] S. L. Gai, C. X. Li, P. P. Yang, J. Lin, *Chem. Rev.* **2014**, *114*, 2343.

[46] a) C. S. Pan, Y. F. Zhu, *Environ. Sci. Technol.* **2010**, *44*, 5570; b) C. C. Chen, Q. Wang, P. X. Lei, W. J. Song, W. H. Ma, J. C. Zhao, *Environ. Sci. Technol.* **2006**, *40*, 3965; c) Y. Yang, Y. Guo, F. Liu, X. Yuan, Y. Guo, S. Zhang, W. Guo, M. Huo, *Appl. Catal. B: Environ.* **2013**, *142*, 828.

[47] J. T. Li, S. K. Cushing, P. Zheng, T. Senty, F. K. Meng, A. D. Bristow, A. Manivannan, N. Q. Wu, *J. Am. Chem. Soc.* **2014**, *136*, 8438.

[48] M. J. Kale, T. Avanesian, P. Christopher, *ACS Catal.* **2014**, *4*, 116.

[49] S. Mubeen, J. Lee, N. Singh, S. Krämer, G. D. Stucky, M. Moskovits, *Nat. Nanotechnol.* **2013**, *8*, 247.

[50] P. Christopher, H. Xin, A. Marimuthu, S. Linic, *Nat. Mater.* **2012**, *11*, 1044.

[51] S. Han, L. Hu, N. Gao, A. A. Al-Ghamdi, X. Fang, *Adv. Funct. Mater.* **2014**, *24*, 3725.

[52] T. C. Choy, *Effective Medium Theory: Principles and Applications,* Oxford University Press, London **1999**.

[53] E. D. Palik, *Handbook of Optical Constants of Solids,* Academic, New York **1985**.